



# Sn–Mn binary metal oxides as non-carbon sorbent for mercury removal in a wide-temperature window



Jiangkun Xie, Haomiao Xu, Zan Qu\*, Wenjun Huang, Wanmiao Chen, Yongpeng Ma, Songjian Zhao, Ping Liu, Naiqiang Yan\*

School of Environmental Science and Engineering, Shanghai Jiao Tong University, Shanghai 200240, China

## ARTICLE INFO

### Article history:

Received 24 January 2014

Accepted 12 April 2014

Available online 24 April 2014

### Keywords:

Sn–Mn binary metal oxide

Mercury adsorbent

Wide temperature window

Mercury stability

## ABSTRACT

A series of Sn–Mn binary metal oxides were prepared through co-precipitation method. The sorbents were characterized by powder X-ray diffraction (powder XRD), transmission electronic microscopy (TEM), H<sub>2</sub>-temperature-programmed reduction (H<sub>2</sub>-TPR) and NH<sub>3</sub>-temperature-programmed desorption (NH<sub>3</sub>-TPD) methods. The capability of the prepared sorbents for mercury adsorption from simulated flue gas was investigated by fixed-bed experiments. Results showed that mercury adsorption on pure SnO<sub>2</sub> particles was negligible in the test temperature range, comparatively, mercury capacity on MnO<sub>x</sub> at low temperature was relative high, but the capacity would decrease significantly when the temperature was elevated. Interestingly, for Sn–Mn binary metal oxide, mercury capacity increased not only at low temperature but also at high temperature. Furthermore, the impact of SO<sub>2</sub> on mercury adsorption capability of Sn–Mn binary metal oxides was also investigated and it was noted that the effect at low temperature was different comparing with that of high temperature. The mechanism was investigated by diffuse reflectance infrared Fourier transform spectroscopy (DRIFTS). Moreover, a mathematic model was built to calculate mercury desorption activation energy from Sn to Mn binary metal oxides.

© 2014 Elsevier Inc. All rights reserved.

## 1. Introduction

Mercury pollution has attracted increasing attention since the notorious Minamata disease occurred in Japan in 1950s. Mercury emission into the environmental exerts long-term threat to ecosystem due to its bio-accumulation and neurotoxicity [1–3]. With the rapid development of society and industrialization, coal-fired power plant has become one of the most important anthropogenic sources for mercury emission. As the largest coal-consuming country in the world, China's mercury emission from coal combustion has been estimated to increase year on year [4] (See Fig. 1).

This deteriorating trend on mercury pollution has attracted worldwide concerns and a series of regulation has or will be implemented including an international treaty on mercury pollution will soon be agreed upon [5]. The US EPA issued the first national standards for mercury pollution from power plants in 2011. China's government has also paid increasing attention to mercury control. In particular, the newly issued "Emission Standard of Air Pollutants for Thermal Power Plants" (GB13223-2011) capped mercury

emissions. To meet these emission standards, new device or process for mercury emissions control is indispensable.

Existing air pollution control devices, including selective catalytic reduction (SCR), electrostatic precipitation (ESP) and flue gas desulfurization (FGD) systems, can remove part of mercury in flue gas [6]. To further reduce the mercury emission from flue gas, activated carbon injection is considered as one of the most important technologies. However, the possible degradation of fly ash which is often used to produce construction material in China and the high cost limit the wide application of activated carbon sorbents. Moreover, most of researches on mercury emission control are focusing on stable work condition (stable temperature), mercury emission during unstable conditions such as during start-up and stop period has been neglected. To capture mercury during these conditions that temperature fluctuated greatly, developing mercury sorbent with good capacity in wide temperature range is very important.

Recently, some reports have shown that non-carbon materials may become promising alternatives as mercury sorbents [7–10]. Due to good reducibility and catalytic activity, manganese oxides have attracted more and more interests in catalytic areas including mercury removal and selective catalytic reduction (SCR) of NO<sub>x</sub> [11–14]. But the specific surface area of single metal manganese oxides is often very low due to their tendency to aggregate.

\* Corresponding authors. Fax: +86 021 54745591.

E-mail addresses: quzan@sjtu.edu.cn (Z. Qu), nqyan@sjtu.edu.cn (N. Yan).

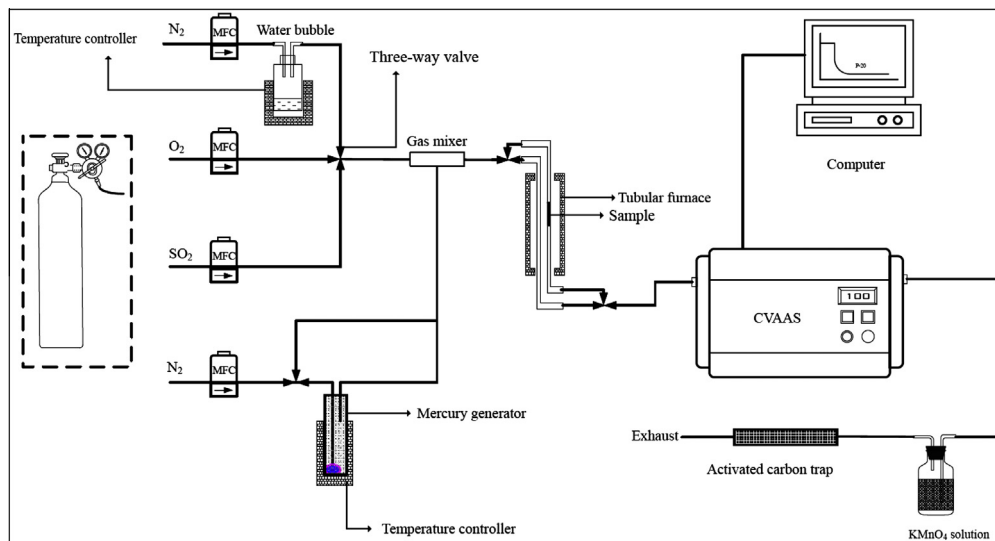


Fig. 1. Sketch of flow process for sorbent mercury capacity evaluation.

Increasing its specific surface area is good for utilizing active component more effectively. It was found that doping was an effective way to increase surface area, and some bimetallic materials had already been developed for catalytic reaction [15]. Tin foil is often used in food package due to its low toxicity, meanwhile, Sn–Mn binary metal oxides has been reported having good SCR activity [11]. But so far as we know, no research about the capability of Sn–Mn binary metal oxides for flue gas mercury removal has been published. Therefore, how Sn–Mn binary metal oxides will performance on flue gas mercury removal attract our interest.

Herein, a series of non-carbon sorbents which can be used in a wider temperature window for mercury removal from flue gas were developed and their mercury adsorption capacities were measured through fix-bed experiment. The impact of  $\text{SO}_2$  on mercury removal ability of the sorbents was also investigated. Based on characterization and breakthrough experiment results, the adsorption mechanism and the impact of main flue gas components were discussed. Moreover, a mathematic model was built to calculate mercury desorption activation energy from Sn to Mn binary metal oxides.

## 2. Experimental section

### 2.1. Sorbent preparation

The sorbents were prepared through the co-precipitation method. The process was briefly described as follows. A given amount of mixed metal nitrates was added to deionized water under stirring until it was completely dissolved, after which the stoichiometric amount of ammonia was added to the solution as the precipitation agent under strong stirring for 2 h. For  $\text{MnO}_x\text{-SnO}_2$  (Mn:Sn = 1:1 mol/mol), 20 mmol of  $\text{SnCl}_4$  and 20 mmol of  $\text{Mn}(\text{NO}_3)_2$  were dissolved in 80 ml of deionized water under stirring, after which 120 mmol of ammonia was added to the mixed solution under strong stirring for 2 h. The precipitate was filtrated and washed with deionized water until no  $\text{Cl}^-$  was detectable in the water, and the precipitate was transferred to a muffle furnace and calcined at 500 °C for 5 h.  $\text{SnO}_2$ ,  $\text{MnO}_x$ ,  $\text{MnO}_x\text{-SnO}_2$  (Mn:Sn = 3:1 mol/mol) and  $\text{MnO}_x\text{-SnO}_2$  (Mn:Sn = 1:3 mol/mol) were prepared using the same procedure except with different amounts of mixed metal nitrates and ammonia. All the samples were ground to 40–60 mesh.

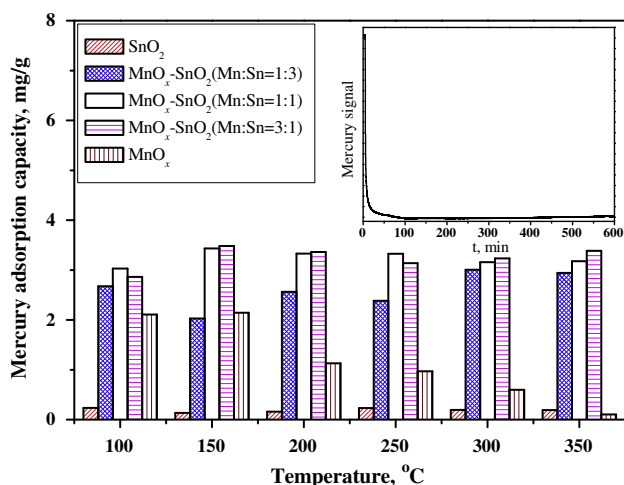


Fig. 2. Impact of temperature on mercury capacity of the prepared sorbents. The inset: the breakthrough curve of  $\text{MnO}_x\text{-SnO}_2$  (Mn:Sn = 1:1) was shown at 150 °C.

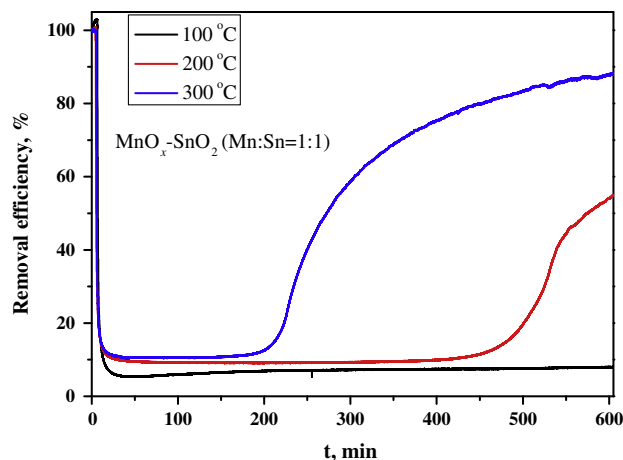


Fig. 3. Impact of  $\text{SO}_2$  on mercury adsorption performance at different temperature test condition: 500 ppm  $\text{SO}_2$  + 4%  $\text{O}_2/\text{N}_2$ .

## 2.2. Sorbent characterization

Powder X-ray diffraction patterns (powder XRD) were performed on a Rigaku D/max-2200/PC powder diffractometer using Cu K $\alpha$  radiation (40 kV and 20 mA). A glass holder was used to support the samples. The scanning range was from 10° to 80° with scanning velocity of 7° min<sup>-1</sup>. The powder XRD phases present in the samples were identified with the help of JCPDS data files corresponding to the file No. 21-1250. The microstructure of catalysts was analyzed by transmission electronic microscopy (TEM). Samples were dispersed in ethanol with strong sonication before analysis, and the data were collected on JEM-2100 (20 kV) with Energy dispersive X-ray spectroscopy (EDX) as an accessory. Nitrogen adsorption and desorption isotherms were obtained on a nitrogen adsorption apparatus (Quantachrome Nova 2200e) at -196 °C (temperature of liquid nitrogen bath). All samples were degassed for 3 h at 200 °C before test. Specific surface areas were calculated through Brunauer–Emmett–Teller (BET) method. H<sub>2</sub>-TPR and NH<sub>3</sub>-TPD experiments were performed on Chemisorp TPx 2920 instrument, the sorbents were degassed at 300 °C for 3 h under Ar atmosphere before H<sub>2</sub>-TPR test, the reducing gas was 10% H<sub>2</sub>/Ar. For NH<sub>3</sub>-TPD test, the sorbent was degassed at 500 °C under He atmosphere and then cooled down to room temperature, the physically adsorbed NH<sub>3</sub> was purged out by He before test. The X-ray photoelectron spectroscopy (XPS) measurements were carried out on an AXIS Ultra<sup>DL</sup> (Shimadzu–Kratos) spectrometer with Al K $\alpha$  as the excitation source. The C 1s line at 284.6 eV was taken as a reference for the binding energy calibration. Diffuse reflectance infrared Fourier transform spectroscopy (DRIFTS) was carried out on a Nicolet 6700 (Thermo Fisher Scientific) Fourier transform infrared spectrometer, the flow rate of influent containing 500 ppm SO<sub>2</sub> + 4% O<sub>2</sub>/N<sub>2</sub> was controlled by mass flow controller, the flow rate was 200 ml min<sup>-1</sup> which was the same as in breakthrough experiment.

## 2.3. Adsorption capacity evaluation

The assembly used for elemental mercury capture consisted of an elemental mercury permeation tube, a packed-bed reactor with a parallel blank tube, a cold vapor atomic absorption spectrometer (CVAAS) and an online data acquisition system. A tubular furnace was employed to control the reactor at desired temperatures. N<sub>2</sub> was used as the carrier gas to yield a stable concentration of elemental mercury. Before test, mercury permeation tube was bypassed to calibrate the signal baseline, and then carrier gas was diverted into mercury permeation tube to generate stable mercury concentration. After that, gaseous influent with stable mercury concentration was diverted into packed-bed reactor and the breakthrough curves were recorded by online data acquisition system. The reactor was packed with a certain amount of sorbents (30 mg), and quartz wool was used as the support to prevent the loss of sorbents. In order to build a mercury balance, a reducing bottle containing SnCl<sub>2</sub> solution was placed on the outlet of the first CVAAS detector, and another CVAAS detector was put in tandem with the first one. It was found that almost the same signal could be obtained by two detectors. It meant that Hg<sup>2+</sup> in the effluent was negligible. Therefore, the influent mercury should be equal to mercury adsorbed on sorbent surface plus elemental mercury in the effluent. The process flow of packed bed experiments is sketched below:

To investigate the effect of flue gas components, the area of breakthrough curves of elemental mercury on Sn–Mn binary oxides during the test time (10 h) was integrated and the adsorption capacities of the mercury were calculated according to Eq. (1). Mercury adsorption capacity was defined as the mass of elemental

mercury that was converted into HgO or other forms on unit mass of sorbent. It was calculated as follows in this experiment:

$$Q = \frac{1}{m} \int_{t_0}^{t_1} (Hg_{inlet}^0 - Hg_{outlet}^0) \times f \times dt \quad (1)$$

where  $Q$  is the mercury adsorption capacity,  $m$  is mass of sorbent in the fixed-bed,  $f$  denotes the flow rate of the influent, and  $t_0$  and  $t_1$  represent the initial and ending test time of the breakthrough curves, respectively.

Herein, the total flow rate of gaseous influent was controlled by mass flow controller at 200 ml min<sup>-1</sup>. The influent contained 0.85 ( $\pm 0.05$ ) mg m<sup>-3</sup> of elemental mercury and 4% O<sub>2</sub> (V/V) and the flow rate was balanced with N<sub>2</sub>. Taking the impact of temperature on adsorption performance into consideration, the tests were carried out at a temperature range from 100 to 350 °C. The gas space velocity was about  $3.2 \times 10^5$  h<sup>-1</sup>. To test the influence of SO<sub>2</sub>, 500 ppm of SO<sub>2</sub> were introduced into the gaseous influent through mass flow controller, and the total flow rate was also balanced with N<sub>2</sub>. The elemental mercury concentrations of gaseous influent and effluent were continuously measured by a CVAAS (SG921, Jiangfen Ltd., China) which was calibrated by Lumex RA 915 + mercury analyzer.

## 3. Results and discussion

### 3.1. Adsorption experiments

The impact of temperature on mercury capacity of the sorbents was investigated through fix-bed experiment. As shown in Fig. 2, pure SnO<sub>2</sub> had negligible mercury capacity at 100–350 °C. Comparatively, mercury adsorption capacity on prepared MnO<sub>x</sub> could reach to 2 mg/g at 100–150 °C, however, the capacity decreased significantly with the increase of temperature. For binary metal oxides, the mercury capacity was relative high (about 3.7 mg/g at 150 °C) comparing with SnO<sub>2</sub> and MnO<sub>x</sub> (the breakthrough curve was shown in the inset, the removal efficiency within 10 h was higher than 95%). It's seemed that manganese content would not impact the mercury capacity significantly, especially when its mole ratio against tin is above 1:1. Moreover, the relative high capacity did not show any decrease at higher temperature. It meant that the prepared Sn–Mn binary metal oxides had the potential to be used at from 100 to 350 °C. According to the results, manganese should be the main active component for mercury adsorption and the interaction between manganese and tin oxides could improve the high temperature activity for mercury capture. In other words, doping of tin is an effective way to enlarge the active temperature window of the sorbent.

### 3.2. Impact of SO<sub>2</sub> on adsorption behavior

SO<sub>2</sub> is the flue gas component which often poisons the catalyst in SCR process. Herein, the impact of SO<sub>2</sub> on mercury capacity of the sorbent at different temperature was studied through fixed-bed experiment. As shown in Fig. 3, MnO<sub>x</sub>–SnO<sub>2</sub> (Mn:Sn = 1:1 mol/mol) displayed very high mercury removal efficiency and did not show any trend to breakthrough at 100 °C within 10 h under the atmosphere of 500 ppm SO<sub>2</sub> + 4% O<sub>2</sub>/N<sub>2</sub>, however, under the same atmosphere, mercury began to breakthrough after about 8 h and 3.5 h at 200 and 300 °C, respectively. This breakthrough might be attributed to the loss of active sites for mercury adsorption. It was speculated that the sorbent interacted with SO<sub>2</sub> more strongly at high temperature, and the formed sulfate species covered the active sites and inhibited the further adsorption of mercury, therefore, the adsorption curve began to breakthrough. But the loss of active sites was much less at low

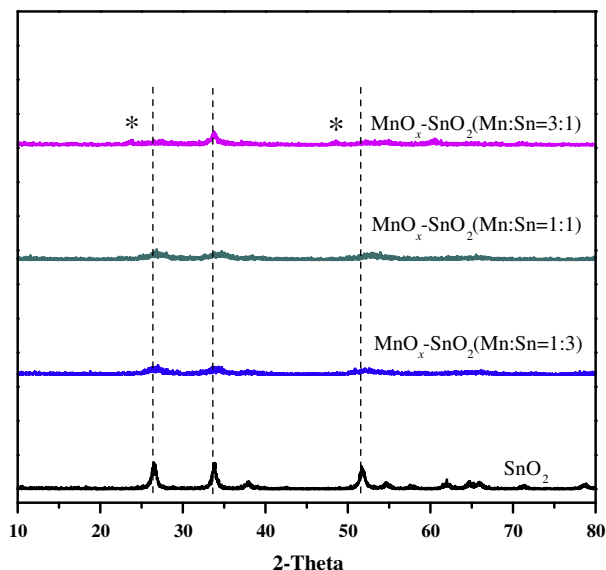


Fig. 4. Powder XRD patterns of prepared  $\text{SnO}_2$  and Sn–Mn binary metal oxides.

temperature. In other words, the sorbent had much better tolerance to  $\text{SO}_2$  at low temperature (The mechanism is discussed below based on DRIFTS result). This better tolerance against  $\text{SO}_2$  will benefit the application of the sorbent for flue gas mercury removal at low temperature.

### 3.3. Characterization of sorbents

To characterize the crystal phase of the sorbents, powder XRD was employed to collect diffraction data. As shown in Fig. 4, the prepared  $\text{SnO}_2$  could be attributed to tetragonal phase (PDF# 21-1250 P42/mmm (136)). It's worth noting that the prepared Sn–Mn binary metal oxides could be attributed to the same crystal structure. With the increase of manganese ratio, half-width of the peaks increased indicating the decrease of the crystal size after doping of manganese. When the manganese ratio against tin was up to 3:1, some small peaks corresponding to manganese oxides began to appear. It was speculated that the formation of Sn–Mn binary metal oxides could inhibit the grain growth and particle aggregation under the preparing condition. Therefore, smaller crystal size tends to be formed for Sn–Mn binary oxides. Furthermore, Scherrer equation was used to calculate the lattice parameter. It was found that peak corresponding to (110) facet emerged at  $2\theta = 26.5^\circ$  for  $\text{SnO}_2$  while this peak for  $\text{MnO}_x\text{-SnO}_2$  (Mn:Sn = 1:1 mol/mol) appeared at  $2\theta = 27^\circ$ . It was speculated that partial manganese doped into the lattice of  $\text{SnO}_2$  and change its lattice parameter, and this was consistent with the Ref. [16].

Transmission electronic microscopy was employed to characterize the morphology of the prepared sorbents. As shown in Fig. 5,  $\text{MnO}_x\text{-SnO}_2$  (Mn:Sn = 1:1 mol/mol) had smaller particle size than  $\text{SnO}_2$ , and its shape seemed to be much more regular. This result matched well with powder XRD data (increase of half-width of the peaks). It was speculated that the formed Sn–Mn binary metal oxides could inhibit the aggregation and grain growth of the particles, therefore, the smaller particle size tended to form. And this smaller size facilitated the exposure of more active sites and increased the contacting opportunity of active sites with mercury molecules. Additionally, by measuring the lattice spacing from the high resolution images, it was found that the lattice spacing corresponding to (110) facet slightly decreased from 0.3222 to 0.3143 nm after doping of manganese indicating partial manganese may doped into  $\text{SnO}_2$  lattice to form solid solution. This result was also consistent with the powder XRD.

Large surface area facilitates the contact between the reactant and sorbent. Herein,  $\text{N}_2$ -adsorption technology was employed to measure the surface area of the prepared sorbents. As shown in Table 1, the specific surface areas for single metal oxides were relative low (only about  $5 \text{ m}^2/\text{g}$  for  $\text{MnO}_x$  and  $25 \text{ m}^2/\text{g}$  for  $\text{SnO}_2$ ). After the formation of binary metal oxides, the specific surface area increase significantly (about  $50 \text{ m}^2/\text{g}$ ). Taking the results of powder XRD and TEM into consideration, the larger specific surface areas of Sn–Mn binary metal oxides were consistent with their broader half-width of the powder XRD peaks and the smaller particle size. It's worth noting that lower surface area material tended to form for  $\text{SnO}_2$  and  $\text{MnO}_x$ , however, after the formation of binary metal oxides, the surface area was doubled. Combining the results of powder XRD, TEM with  $\text{N}_2$ -adsorption data, it was speculated that the interaction between Sn and Mn inhibited the grain growth and particle aggregation and facilitated the formation of small size particles.

To characterize the reducibility of the prepared sorbents,  $\text{H}_2$ -TPR technology was employed to collect the reducing information during the temperature-programmed process. The results were shown in Fig. S1, the reducing peak of single metal oxide  $\text{SnO}_2$  emerged at higher than  $600^\circ\text{C}$  demonstrating the reducibility of single tin oxides was relative weak. With the addition of manganese, a new reducing peaks of formed Sn–Mn binary metal oxides appeared at  $200\text{--}400^\circ\text{C}$ . Furthermore, the reducing peak corresponding to  $\text{SnO}_2$  split into two peaks indicating the existence of the interaction between Sn and Mn in the binary metal oxides. With further increase of manganese content, the reducing peaks at low temperature became stronger and the amount of hydrogen consumption at low temperature increased indicating the enhancement of reducibility of the binary metal oxides comparing with  $\text{SnO}_2$ . Moreover, with the increase of manganese, the peaks at low temperature became a little complicated. It was speculated that different valences of manganese species were formed on the sorbent surface. But according to powder XRD result, no obvious

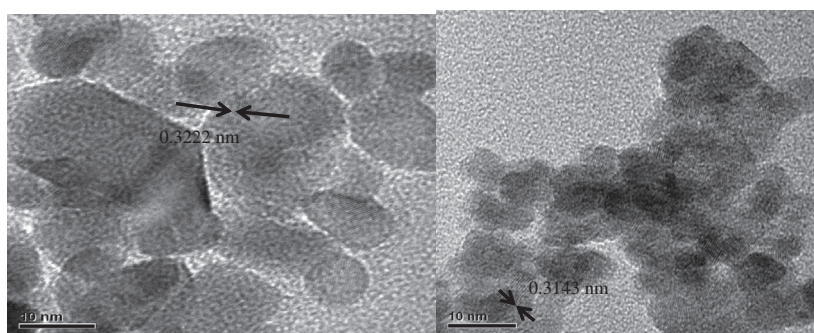
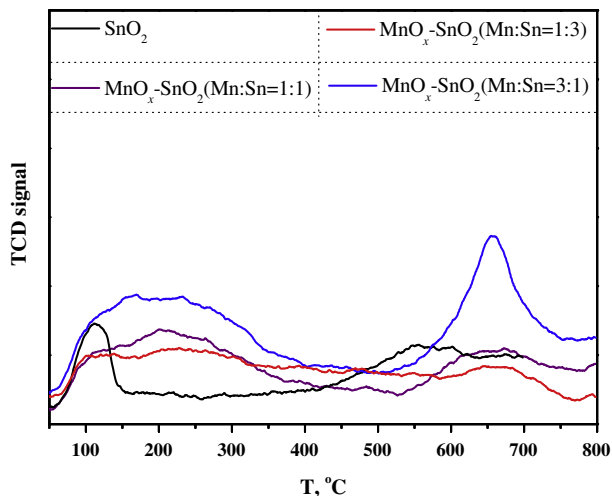


Fig. 5. Transmission electronic microscopy images of  $\text{SnO}_2$  (left) and  $\text{MnO}_x\text{-SnO}_2$  (Mn:Sn = 1:1 mol/mol) (right).

**Table 1**  
BET specific surface area of the prepared sorbent obtained from N<sub>2</sub> adsorption test.

Sample	SnO <sub>2</sub>	MnO <sub>x</sub> -SnO <sub>2</sub> (Mn:Sn = 1:3)	MnO <sub>x</sub> -SnO <sub>2</sub> (Mn:Sn = 1:1)	MnO <sub>x</sub> -SnO <sub>2</sub> (Mn:Sn = 3:1)	MnO <sub>x</sub>
BET surface area, m <sup>2</sup> /g	25.5	47.9	54.0	49.8	5.3



**Fig. 6.** NH<sub>3</sub>-TPD curves of the prepared Sn-Mn binary metal oxides.

peak corresponding manganese oxides could be observed when the manganese ratio against tin was below 1:1, it could be speculated that some amorphous MnO<sub>x</sub> formed on the sorbent surface or the formed MnO<sub>x</sub> on the surface was below the detection limit of

powder XRD. In sum, the doping of manganese increased the reducibility of the sorbent and provided the potential ability to oxidize elemental mercury adsorbed on the sorbent surface.

As the electron of Hg 4f tend to be attracted by other element, Hg is often considered as Lewis base. Therefore, the acidity of the sorbent is very important for its mercury adsorption performance. Herein, NH<sub>3</sub>-TPD test was employed to test the strength of acidity on the sorbents' surface. As shown in Fig. 6, the desorption peaks of NH<sub>3</sub> on SnO<sub>2</sub> emerged at about 100 and 550 °C indicating there's two kind of acidic sites on the sorbent's surface. After doping of manganese, both peak centers shifted toward high temperature. It illustrated that the doping of manganese could significantly enhance the strength of acidity. Furthermore, the desorption peaks of NH<sub>3</sub> on the sorbent were also broadened after doping of manganese. It demonstrated that more acidic sites with different acidic strength were formed on the sorbent surface. In one word, the doping of manganese not only enhanced the acidic strength of the sorbent but also increased the acidic sites on the sorbent surface. This may play a very important role on mercury adsorption performance.

XPS was employed to analyze mercury species on sorbent surface. As shown in Fig. S2, there's no peak corresponding to mercury could be observed on fresh sorbent surface. After adsorbing mercury in N<sub>2</sub> and 4% O<sub>2</sub>, the XPS peaks emerged at 105.0 and 101.0 eV which could be attributed to Hg 4f 5/2 and 7/2, respectively. It meant that the formed mercury species was HgO. After

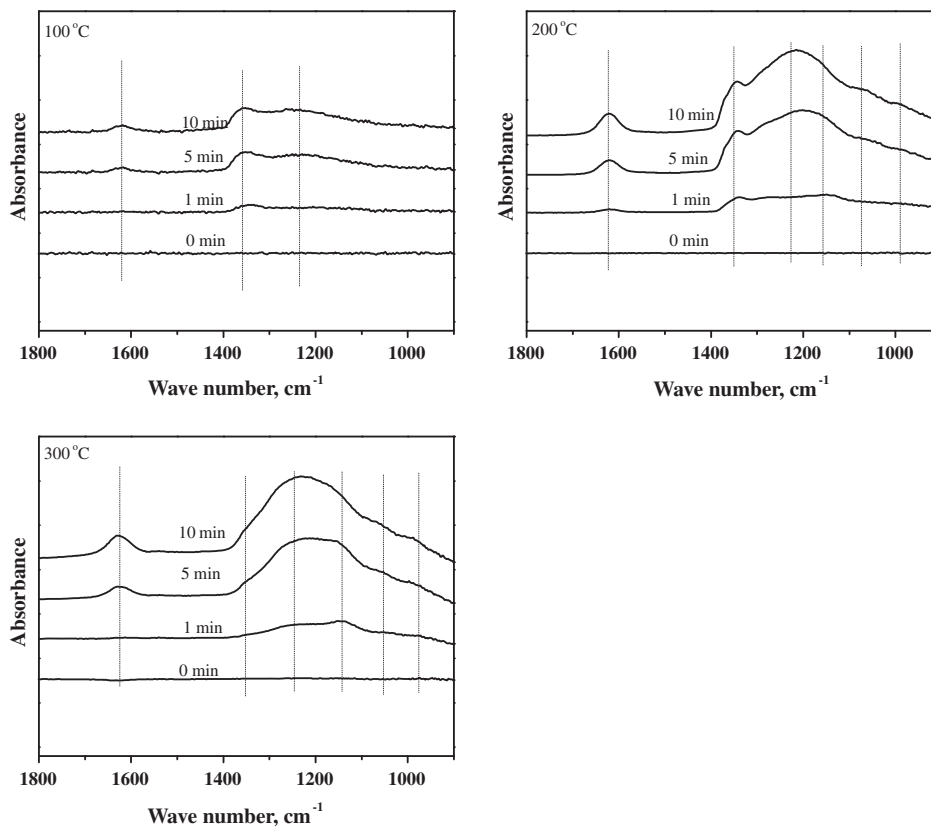


**Fig. 7.** Interaction between SO<sub>2</sub> and MnO<sub>x</sub>-SnO<sub>2</sub> (Mn:Sn = 1:1) tested by in situ DRIFTS Test condition: 500 ppm SO<sub>2</sub> + 4% O<sub>2</sub>/N<sub>2</sub>.

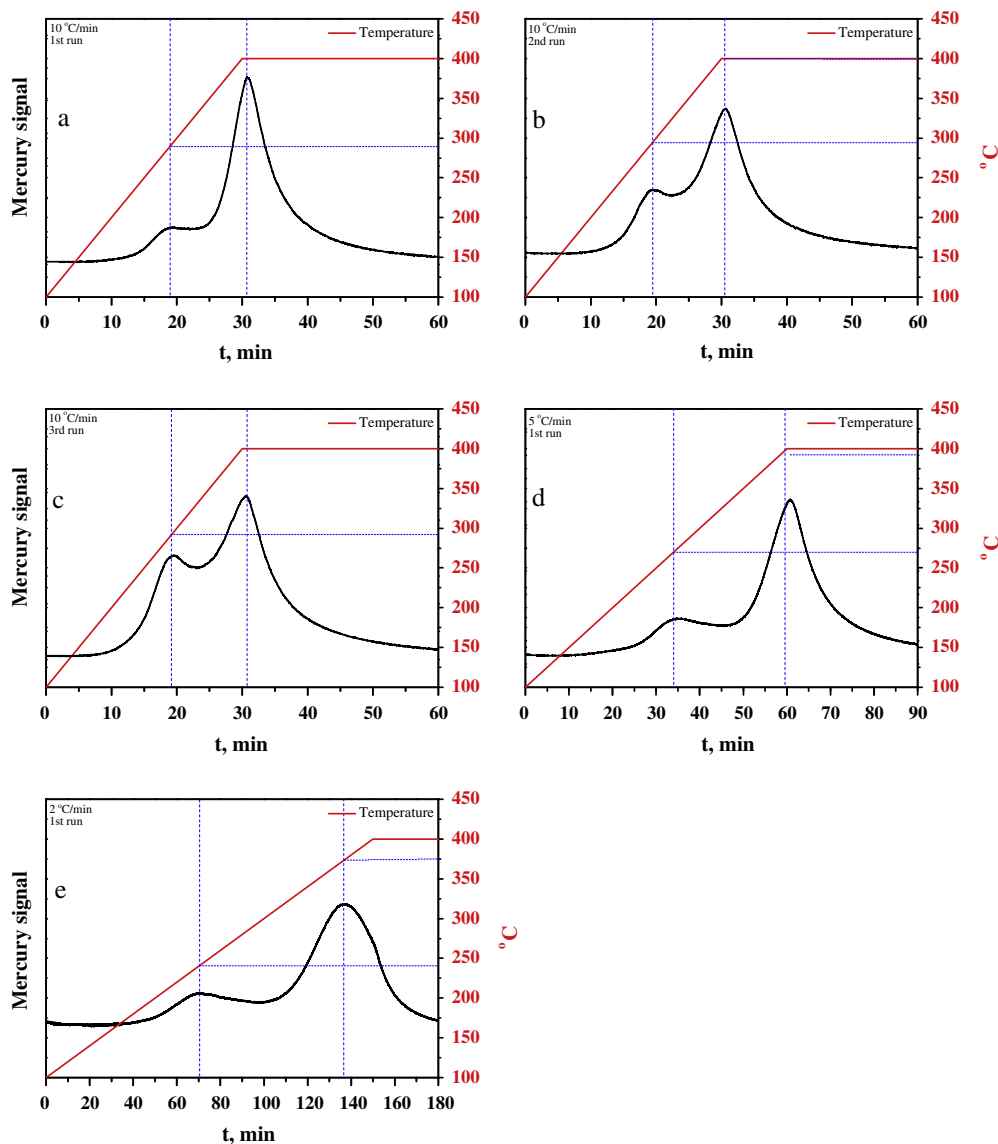


Fig. 8. Hg-TPD curves on  $\text{MnO}_x\text{-SnO}_2$  (Mn:Sn = 1:1) at different heating rate.

adsorbing mercury in  $\text{N}_2$ , 4%  $\text{O}_2$  and 500 ppm  $\text{SO}_2$ , the XPS peaks displayed a slight shift and emerged at 105.3 and 101.3 eV. The formed mercury species was also  $\text{HgO}$  [12]. And the slight shift may be attributed to the interaction between  $\text{HgO}$  and the metal sulfate. It was speculated that mercury was firstly adsorbed on sorbent's surface, and then was oxidized to  $\text{HgO}$  and covered the sorbent surface. With the increase of surface  $\text{HgO}$ , the mercury adsorption ability will decrease and the breakthrough curve will begin to show the trend to breakthrough.

As mentioned above,  $\text{SO}_2$  could inhibit mercury adsorption on Sn–Mn binary metal oxides at high temperature, but the impact decreased significantly at low temperature. To further investigate the mechanism for impact of  $\text{SO}_2$  at different temperature, diffuse reflectance infrared Fourier transform spectroscopy was employed to collect the in situ spectra data. Fig. 7 showed the spectra at different temperature when sample was exposed to 500 ppm  $\text{SO}_2 + 4\%\text{O}_2/\text{N}_2$  for different time. Several peaks at 1344, 1278, 1149, 1050 and  $976\text{ cm}^{-1}$  emerged and the intensity increased with the exposure time. The peak at  $1344\text{ cm}^{-1}$  could be attributed to  $\nu(\text{S}=\text{O})$  vibration of surface sulfate species with only one  $\text{S}=\text{O}$  band. Peaks at 1278, 1149, 1050 and  $976\text{ cm}^{-1}$  could be assigned

to the stretching motion of adsorbed bisulfate or sulfate on the surface of the sample [17–21]. Interestingly, it was found that more sulfate species could be found when the sample was exposed to  $\text{SO}_2$  at high temperature. By contrast, lower intensity of sulfate related peaks could be observed at low temperature. It was speculated that the interaction between sample and  $\text{SO}_2$  was determined by two steps: adsorption and reaction. Low temperature facilitated the adsorption and high temperature promotes the reaction activity. In this case, the activity was the key step for reaction between  $\text{SO}_2$  and the sample. Therefore, low temperature inhibited the reaction between  $\text{SO}_2$  and the sample and prevented the sample from poisoning by  $\text{SO}_2$ .

#### 3.4. Mercury desorption from sorbent surface

Moreover, to further investigate the desorption performance of mercury from the sorbent, mercury temperature-programmed desorption (Hg-TPD) curves under different heating rate on  $\text{MnO}_x\text{-SnO}_2$  (Mn:Sn = 1:1 mol/mol) surface were collected and the results were shown in Fig. 8. It could be found that two peaks emerged during desorption process. This indicated there were two kind of

adsorption sites on the sorbent's surface. The higher temperature the desorption peak appeared at, the stronger the interaction force between mercury and adsorption sites was. It's worth noting that two desorption peaks appeared when the adsorption was carried out under N<sub>2</sub> and O<sub>2</sub> condition (without SO<sub>2</sub>), however, if the adsorption was performed under N<sub>2</sub> + O<sub>2</sub> + 500 ppm SO<sub>2</sub> condition (with SO<sub>2</sub>), desorption peaks disappeared (Fig. S3). It meant SO<sub>2</sub> could strengthen the interaction between mercury and sorbent which would reduce the risk of mercury re-emission.

### 3.5. Building of a model for calculation of mercury desorption activation energy

Meanwhile, it was found that heating rate could impact the desorption behavior of mercury from sorbent surface. The faster the heating rate was, the higher temperature the desorption peaks appeared at. Based on the desorption data, the desorption activation energy was calculated according to Eq. (S-7) (see supporting information for more details). They were 67.0 and 158.2 kJ/mol corresponding to 1st peak and 2nd peak, respectively (Table S-1).

$$2 \ln T_p - \ln \beta = \frac{E_d}{RT_p} + \ln \frac{E_d}{AR} \quad (\text{S-7})$$

## 4. Conclusion

In conclusion, a series of Sn–Mn binary metal oxides was prepared and investigated for flue gas mercury removal. It was found that pure SnO<sub>2</sub> had negligible mercury capacity at test temperature while Sn–Mn binary metal oxides had much higher mercury capacity in a wide temperature window (from 100 to 350 °C). Mercury firstly adsorbed on the sorbent surface and then was oxidized into HgO by Sn–Mn metal oxides and covered sorbent surface. It was speculated that following reasons contributed to the enhancing mercury removal ability: 1. Higher specific surface area after doping of manganese provided more chances for mercury to interact with active sites on sorbents' surface. 2. The boosted acidic strength increased the ability of the sorbent to capture mercury from flue gas. 3. The enhanced reducibility promoted the activity of the sorbent to oxidize the adsorbed mercury. It was also found that SO<sub>2</sub> has negative effect for mercury capture on Sn–Mn binary metal oxides at high temperature. Comparatively, the tolerance of sorbent toward SO<sub>2</sub> at low temperature was much better. Furthermore, mercury desorption activation energies from Sn to Mn

binary metal oxides were 67 and 158.2 corresponding to two kind of adsorption sites.

## Acknowledgments

This study was supported by the Major State Basic Research Development Program of China (973 Program, No. 2013CB430005), the National Natural Science Foundation of China, China (No. 21277088) and the National High-Tech R&D Program (863) of China (Nos. 2011AA060801, 2013AA065403). Professor Shijian Yang was thanked for helpful discussion.

## Appendix A. Supplementary material

Supplementary data associated with this article can be found, in the online version, at <http://dx.doi.org/10.1016/j.jcis.2014.04.032>.

## References

- [1] E.G. Pacyna, J.M. Pacyna, K. Sundseth, J. Munthe, K. Kindbom, S. Wilson, F. Steenhuisen, P. Maxson, *Atmos. Environ.* 44 (2010) 2487–2499.
- [2] D.G. Streets, Q. Zhang, Y. Wu, *Environ. Sci. Technol.* 43 (2009) 2983–2988.
- [3] W.F. Fitzgerald, C.H. Lamborg, C.R. Hammerschmidt, *Chem. Rev.* 107 (2007) 641–662.
- [4] G.B. Jiang, J.B. Shi, X.B. Feng, *Environ. Sci. Technol.* 40 (2006) 3672–3678.
- [5] M. Rallo, M.A. Lopez-Anton, M.L. Contreras, M.M. Maroto-Valer, *Environ. Sci. Pollut. R.* 19 (2012) 1084–1096.
- [6] A.A. Presto, E.J. Granite, *Environ. Sci. Technol.* 40 (2006) 5601–5609.
- [7] J. Dong, Z.H. Xu, S.M. Kuznicki, *Environ. Sci. Technol.* 43 (2009) 3266–3271.
- [8] F. Scala, C. Anacletia, S. Cimino, *Fuel* 108 (2013) 13–18.
- [9] M.A. Abu-Daibes, N.G. Pinto, *Chem. Eng. Sci.* 60 (2005) 1901–1910.
- [10] L. Zhang, Y.Q. Zhuo, W. Du, Y. Tao, C.H. Chen, X.C. Xu, *Ind. Eng. Chem. Res.* 51 (2012) 5292–5298.
- [11] X.F. Tang, J.H. Li, L.S. Wei, J.L. Hao, *Chin. J. Catal.* 29 (2008) 531–536.
- [12] S.J. Yang, N.Q. Yan, Y.F. Guo, D.Q. Wu, H.P. He, Z. Qu, J.F. Li, Q. Zhou, J.P. Jia, *Environ. Sci. Technol.* 45 (2011) 1540–1546.
- [13] L. Ji, P.M. Sreekanth, P.G. Smirniotis, S.W. Thiel, N.G. Pinto, *Energ. Fuel* 22 (2008) 2299–2306.
- [14] F. Wang, H.X. Dai, J.G. Deng, G.M. Bai, K.M. Ji, Y.X. Liu, *Environ. Sci. Technol.* 46 (2012) 4034–4041.
- [15] M. Sankar, N. Dimitratos, P.J. Miedziak, P.P. Wells, C.J. Kiely, G.J. Hutchings, *Chem. Soc. Rev.* 41 (2012) 8099–8139.
- [16] L.S. Wei, J.H. Li, X.F. Tang, *Catal. Lett.* 127 (2009) 107–112.
- [17] B.Q. Jiang, Z.B. Wu, Y. Liu, S.C. Lee, W.K. Ho, *J. Phys. Chem. C* 114 (2010) 4961–4965.
- [18] Y.W. Lee, J.W. Park, J.H. Choung, D.K. Choi, *Environ. Sci. Technol.* 36 (2002) 1086–1092.
- [19] R. Zhang, H. Alamdari, S. Kaliaguine, *Appl. Catal. A – Gen.* 340 (2008) 140–151.
- [20] C. Liu, Q.X. Ma, Y.C. Liu, J.Z. Ma, H. He, *Phys. Chem. Chem. Phys.* 14 (2012) 1668–1676.
- [21] H.Z. Chang, X.Y. Chen, J.H. Li, L. Ma, C.Z. Wang, C.X. Liu, J.W. Schwank, J.M. Hao, *Environ. Sci. Technol.* 47 (2013) 5294–5301.